Combustion and Flame 205 (2019) 55–67

Contents lists available at ScienceDirect

Combustion and Flame

journal homepage: www.elsevier.com/locate/combustflame

Microgravity diffusion flame spread over a thick solid in step-changed low-velocity opposed flows

Feng Zhu[a,b], Zhanbin Lu[c,d], Shuangfeng Wang[a,b,*], Yongli Yin[e]

[a] Key Laboratory of Microgravity, Institute of Mechanics, Chinese Academy of Sciences, Beijing 100190, China
[b] School of Engineering Science, University of Chinese Academy of Sciences, Beijing 100049, China
[c] Institute of Applied Mathematics and Mechanics, Shanghai University, Shanghai 200072, China
[d] Shanghai Key Laboratory of Mechanics in Energy Engineering, Shanghai 200072, China
[e] China Astronaut Research and Training Center, Beijing 100094, China

ARTICLE INFO

Article history:
Received 28 December 2018
Revised 30 January 2019
Accepted 27 March 2019

Keywords:
Opposed-flow flame spread
Thick solid
Microgravity
Radiation-controlled regime
Diffusive-thermal instability

ABSTRACT

We report results from a microgravity combustion experiment conducted aboard the SJ-10 satellite of China, focusing on the structure and dynamics of diffusion flames spreading over a thick PMMA in low-velocity opposed flows. The width of the PMMA sample is chosen to be as large as possible in order to minimize the side diffusion effects of oxygen, and for each of the four oxygen concentration cases considered, four decrementally changing gas flow velocities are imposed such that a wide range of parameter values are spanned near the quenching limit. Two distinct flame spread modes are identified near the quenching limit, namely the continuous flame mode for gas flow velocities greater than an oxygen-concentration dependent critical value, and the flamelet mode for subcritical gas flow velocities. The transition process between these two spread modes due to a step change in the gas flow velocity is usually accompanied by flame oscillations, and diffusive-thermal instability of the leading flame front is identified as the mechanism controlling such transition. A correlation of the flame spread rate data among different oxygen concentrations indicates that, in the presently considered radiation-controlled regime the normalized flame spread rate deviates from the predictions of the thermal theory and decreases monotonically with the increase in the flame Damköhler number. Meanwhile, with the decrease in the flame spread rate, the standoff distance and the inclination angle at the flame leading edge show an increasing and decreasing trend, respectively. An energy balance analysis across the fuel surface beneath the flame leading edge indicates that the variation of the heat absorbed by the solid for vaporization is sub-linear with respect to the flame spread rate, thereby implying that the fuel regression depth has a tendency to increase with decreasing flame spread rate. Moreover, the energy balance analysis suggests that the quenching boundary and the marginal stability boundary identified on the flammability map are, respectively, intrinsically associated with a certain specific ratio of the overall heat losses to the total heat conducted from the flame, or equivalently, associated with a certain specific value of the flame spread rate.

1. Introduction

The research interests in diffusion flames sustained over the surfaces of condensed fuels originate primarily from fire safety concerns [1–3]. The pioneering work of Emmons [4] on diffusion flame combustion in boundary layer flows over liquid fuels brought into attention the significant role played by the mass transfer number, which essentially measures the ratio between the reaction heat generated in the gas stream and the heat consumed at the fuel surface. With the subsequent incorporation of the radiative heat loss effects, the modified mass transfer number has been exploited to evaluate the excess pyrolyzate, from which the flame length can be estimated [5]. Further, as a quantifiable property characterizing the burning propensity of a fuel, the mass transfer number has been proposed to replace the on/off screening criterion to rank material flammability in material screening tests [6,7].

Besides the static combustion configuration pioneered by Emmons, another fire risk associated with condensed fuel combustion is concerned with the spreading of diffusion flames over the fuel surface. In this connection, the seminal work of de Ris [8] constitutes one of the earliest and most important contributions

* Corresponding author at: Key Laboratory of Microgravity, Institute of Mechanics, Chinese Academy of Sciences, Beijing 100190, China.
E-mail address: sfwang@imech.ac.cn (S. Wang).

https://doi.org/10.1016/j.combustflame.2019.03.040
0010-2180/

to the understanding of the physical mechanisms underlying opposed-flow diffusion flame spread over solid fuels. By introducing some necessary assumptions/simplifications, he obtained closed-form analytical solutions for the flame spread rate under both thermally-thin and thermally-thick limiting conditions. These solutions provide important insight into the controlling mechanisms of opposed-flow flame spread over solid fuels within the so-called thermal regime.

Subsequently, many efforts have been made to validate de Ris's formula or to extend his results to more realistic situations by relaxing the aforementioned assumptions and simplifications made in his theory (see, e.g., the review by Fernandez-Pello and Hirano [9], Wichman [10] and T'ien et al. [11]). So far as thick solid fuels—the focus of the present work—are concerned, the simplified analysis of Wichman and Williams [12] reproduced de Ris's formula by replacing the diffusion flame with a semi-infinite, isothermal, line heating source settled on the vaporizing fuel surface, thereby substantiating the view that the thermal regime of flame spread is dominated solely by the heat transfer processes occurring in both the gas and the solid phases. Similar interpretation of the spreading mechanism of diffusion flames over thick solid fuels was arrived at through a qualitative analysis by Bhattacharjee et al. [13], who numerically verified de Ris's analytical formula under a wide variety of ambient conditions and demonstrated that, for thick solid fuels, the flame leading edge coincides with the inception point of fuel vaporization and the entire diffusion flame essentially stays attached to the vaporizing fuel surface. Bhattacharjee et al. [14] systematically assessed the influence of the assumptions and simplifications adopted in de Ris's theory on flame spread rate prediction for thick solids, and proposed a modified formula for the spread rate based on an extended simplified theory.

The thermal regime is no longer adequate to describe the flame spread process when the gas flow velocity becomes so high that finite-rate kinetics begins to play a dominant role [15]. By contrast, near the opposite limit, which is generally characterized by very low flow velocities, radiative heat loss effects become progressively more pronounced with decreasing gas velocity. As a consequence, within such a radiation-controlled regime the flame spread rate deviates from the predictions of the thermal theory and a quenching limit develops at a finite gas flow velocity, the magnitude of which is dependent upon the oxygen concentration and the thickness of the solid fuel [16,17].

The gas flow velocity characteristic of the radiation-controlled regime is in general smaller than the characteristic buoyancy convection velocity, thereby justifying the requirement of a microgravity environment for flame spread experimentation in low-velocity opposed flows. In a series of microgravity experiments aboard the space shuttle [18,19], it was found that, regardless of the ambient oxygen concentration, the flame spread process over thick PMMA in a quiescent atmosphere is inherently unsteady and flame extinction occurs eventually, the mechanism of which may be accounted for by the mismatch between the length scales associated with thermal and mass diffusion. In a microgravity experiment aboard a sounding rocket, Vietoris et al. [20] examined the opposed-flow flame spread process over a thick PMMA in 40% O_2, at three step-changing gas flow velocities that correspond to the strong propagation regime, the transitional regime, and the extinction regime, respectively. Olson et al. [21] reported sounding rocket experimental results of opposed-flow flame spread over thick PMMA under different conditions of oxygen concentration, gas flow velocity, and external radiant heat flux. Notably, external radiant heat flux was found to have dual effects on flame spread, and its overall effect is therefore nonlinear and dependent on the imposed flux level.

Recently, by using a horizontally placed narrow channel apparatus to simulate the microgravity environment, Zhu et al. [22] compared the flame spread characteristics over thick PMMA under both opposed and concurrent flow conditions, and determined the flammability boundaries for each spread configuration. In a normal-gravity experiment conducted in a vertically placed narrow channel, Matsuoka et al. [23] examined downward flame spread between thick PMMA plates in pure-oxygen opposed flows, and observed the formation of isolated flamelets near the quenching limit, the mechanism of which was attributed to the diffusive-thermal instability of the flame fronts. Several recent microgravity flame spread experiments with thick fuels have been conducted either aboard a spacecraft or in the International Space Station (ISS), with the focus on the characteristics of flame spread over PMMA cylinders [24], the pressure effects on concurrent flame spread [25], and the buoyancy and scale effects on concurrent (upward) flame spread [26], respectively.

The objective of the present experimental study is to gain insight into the intrinsic extinction mechanisms of diffusion flames spreading against a forced oxidizer flow over thick solid fuels, as well as to gain a more comprehensive understanding of the structural and dynamical characteristics of the diffusion flames near the extinction limit. Our interest is primarily focused on the low-velocity radiation-controlled regime, and therefore a microgravity environment is a necessity. Among the above-mentioned few actual microgravity experiments on opposed-flow flame spread over flat thick fuels, with the exception of the work of Vietoris et al. [20], almost all experiments used very narrow fuel samples. Such a choice brings about significant side diffusion effects of oxygen [27–29], and therefore tends to underestimate the flammability limit. On the other hand, the choice of narrow fuel samples precludes the possibility of exploring flame instabilities and other characteristic large-scale flame behaviors, which are more inclined to occur within the radiation-controlled regime and may considerably expand the flammability limit. Although Vietoris et al. [20] used a relatively wide fuel, they considered only one oxygen concentration and three flow velocities, and even the lowest flow velocity was still not sufficiently close to the extinction limit to trigger flame instability (see Fig. 6 below).

To address the deficiencies described above, we report in this work microgravity experimental results from the mission "Ignition and Burning of Solid Materials in Microgravity", which was performed aboard the SJ-10 satellite of China in April, 2016 [30,31]. The sample size and testing procedure essentially follow Vietoris et al. [20], but a more comprehensive range of oxygen concentrations and gas flow velocities are covered near the quenching limit.

2. Experiment

The microgravity flame spread experiment was conducted in a specifically designed 39-L combustion chamber, which has eight parallel-arranged, equal-sized flow tunnels, each having a length of 120 mm and a lateral cross section of 95 mm $\times$ 95 mm. Among the eight flow tunnels, four were used to conduct the experiment reported in this paper. A picture from the cross-sectional view of the four flow tunnels is shown in Fig. 1. In each of the four flow tunnels, an aluminum sample holder is mounted on the tunnel wall, and a cast PMMA sample is embedded within the sample holder such that the sample upper surface is flush with the sample holder, as is schematically shown in Fig. 2. The PMMA sample is 61.6 mm long, 50 mm wide and 10 mm thick, a choice of dimensions that essentially follows Ref. [20]. All the gaps between the sample and the holder are filled with mica for the purpose of thermal insulation.

The forced oxidizer flow over the sample surface is driven by a fan installed at the downstream end of the tunnel, which can generate a uniform gas flow with velocity ranging from 0 to 12 cm/s. An aluminum honeycomb gas diffuser is mounted at the upstream

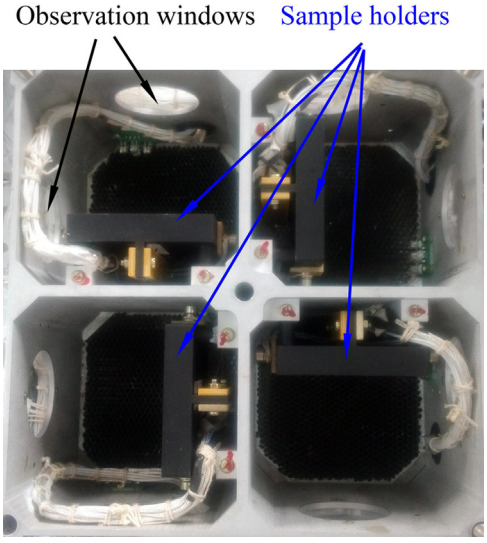

Fig. 1. Cross-sectional view of the flow tunnels inside the combustion chamber.

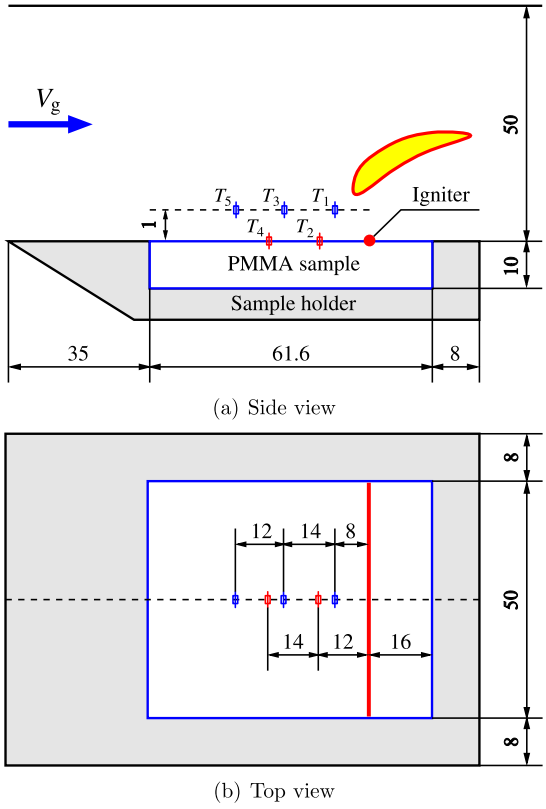

Fig. 2. Schematic diagrams showing the side and top view of the experimental configuration for opposed-flow flame spread over a thick PMMA fuel. Five thermocouples, numbered T_1–T_5, are positioned along the streamwise centerline. All dimensions are in millimeters.

end of the tunnel to ensure uniformity of the incoming flow. The bulk cold flow velocity was calibrated using a Laser Doppler Velocimeter (LDV), and the smoothness of the flow was verified by means of smoke flow visualization in ground tests. A resistively heated coil of ignition wire, which is partially embedded in a small pre-cut notch on the sample surface at a distance of 16 mm away from the downstream edge of the sample, is used as an igniter to initiate the flame. Five thermocouples (type-R, 0.075 mm in diameter), which are numbered T_1–T_5 and positioned along the streamwise centerline of the sample, are used for temperature measurement. As is shown in Fig. 2, T_1, T_3 and T_5 are positioned 1 mm above the sample surface and thus measure the gas phase temperature, whereas T_2 and T_4 are positioned on the sample surface and thus measure the surface temperature of the sample. Two color CCD cameras with a frame rate of 25 fps are used to record the flame spread process from top and side view, respectively, through the two observation windows on the tunnel walls (see Fig. 1).

Two 2.1-L gas bottles charged with O_2/N_2 mixtures were equipped outside the combustion chamber to provide the oxidizing atmosphere during the orbital experiment. The mixtures in the two bottles have an oxygen concentration (by volume) of 21% and 50%, respectively, so by appropriate blending of the two mixtures the oxygen concentration of the oxidizing atmosphere can be continuously varied in the range within these two bounds. At the beginning of each test, residual gas in the chamber is first vented to the vacuum of outer space. Then, once the chamber pressure drops below a sufficiently low value (0.5 kPa was taken in the experiment), gas from the two bottles is filled into the chamber separately according to a specified pressure proportion (corresponding to a specified oxygen concentration), until the chamber pressure reaches 101 kPa. After the gas filling procedure, all the fans in the chamber are switched on and keep running for 8 min to ensure thorough mixing. The chamber pressure is monitored by a pressure sensor, and the real time oxygen concentration in the chamber is monitored by an oxygen sensor. A K-type thermocouple is used to monitor the ambient temperature inside the chamber.

Four opposed-flow flame spread tests were performed during the orbital flight, corresponding to four different ambient oxygen concentrations, i.e., 40%, 35%, 30%, and 25%. Note that the maximum oxygen concentration (40%) corresponds to that used in Ref. [20], whereas the remaining three lower ones are chosen in an attempt to examine the spreading behavior of diffusion flames in regularly descending oxygen concentration atmospheres. The four tests were performed separately; that is, a new test was not started until the previous test was finished. The operation procedure of each test is described as follows. Following the mixture blending procedure and the establishment of a steady-state gas flow with a main stream velocity $V_g = 9$ cm/s, the igniter is switched on and a diffusion flame is initiated over the sample surface. Twenty seconds later, the igniter is switched off and the flame spread starts to be driven alone by the opposed gas flow. During the subsequent flame spread process, the gas flow velocity undergoes three times of step change, each time by a drop of 3 cm/s, until eventually stepping down to 0. Compared to Ref. [20], which used three step-changing flow velocities (15, 10 and 5 cm/s), the present experiment chooses a lower and smaller velocity range with yet denser changing steps, in order to thoroughly examine the flame spreading behavior within the transitional and extinction regimes identified in Ref. [20]. Table 1 lists the time duration corresponding to each gas flow velocity during the four tests. Note that for each oxygen concentration we have set aside a sufficiently long time (> 15 min) for vanishing gas flow velocity, in order to examine the flame spread behavior in quiescent atmospheres.

All the four tests were performed under the identical initial conditions of chamber pressure ($p_a = 101$ kPa) and temperature ($T_a = 285$ K). The variation of these environment parameters (including the oxygen concentration) during the tests was generally very small compared to the initial values. Specifically, the maximum change was found to occur at 40% O_2, in which case after the test there was a pressure rise of 1.4 kPa, an oxygen content decrease of 2.1%, and an ambient temperature increase of 3 K. Such small changes are not expected to have a significant influence, and therefore the flame spread processes can be regarded as proceeding under essentially constant atmospheric conditions.

Table 1
Time duration corresponding to each gas flow velocity during the four flame spread tests at different oxygen concentrations.

Oxygen concentration C_a	Gas flow velocity V_g (cm/s)	Time duration (s)
40%	9	60
	6	50
	3	150
	0	> 900
35%	9	55
	6	40
	3	90
	0	> 900
30%	9	80
	6	80
	3	120
	0	> 900
25%	9	90
	6	90
	3	150
	0	> 900

3. Results and discussions

3.1. Phenomenological description of the flame spread processes

As mentioned in the preceding section (see also Fig. 2), the igniter is positioned 16 mm away from the downstream edge of the PMMA sample. Such an arrangement is intended to examine whether two *separate* flame fronts, one spreading upstream and the other spreading downstream, could develop simultaneously over a thick solid fuel following central ignition, as has been observed for thin fuels at sufficiently high gas flow velocities [32]. It turns out that, in the present microgravity experiment, up to 40%O_2 and gas flow velocity $V_g = 9$ cm/s, following central ignition only upstream spreading flame fronts developed and no separate, downstream spreading flame fronts behind the upstream ones were observed. This finding supports the postulation of Prasad et al. [32] that simultaneous existence of two oppositely spreading diffusion flame fronts might not be possible for thick fuels. The reason, as suggested by Prasad et al. [32], may simply lie in the fact that, unlike thermally thin fuels, fuel depletion (or burnout) does not occur beneath diffusion flames established over thick fuels, so a continuous flame shape will be maintained.

3.1.1. Steady states of flame spread

Figure 3 shows flame images captured from top and side view during the opposed-flow flame spread processes at oxygen concentrations $C_a = 40\%$, 35%, and 30%, under gas flow velocities $V_g =$ 9, 6, and 3 cm/s, respectively. These images were taken after the transients due to ignition or transition between different gas flow velocities were appreciably damped out, and therefore represent steady states of flame spread at the corresponding gas flow velocities.

At 40%O_2, $V_g = 9$ and 6 cm/s, the flame front remains continuous but is apparently nonuniform in terms of luminance along the lateral direction—the two sides appear to be brighter than the middle part of the flame, signifying higher temperature and reactivity at the sides than in the middle. Such nonuniformity may be attributed to the side diffusion effects of oxygen [27–29], which become progressively more pronounced with decreasing gas flow velocity. When V_g is further reduced to 3 cm/s, the flame eventually splits in the middle into two egg-shaped flamelets, which are essentially equal-sized and distribute symmetrically with respect to the streamwise centerline. These two flamelets eventually extinguish when V_g is reduced to 0. The corresponding side-view images show that the flame becomes less bright and more flattened with the decrease in V_g.

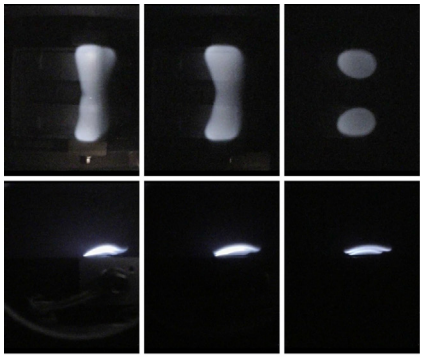

(a) 40% O_2, V_g = 9, 6, and 3 cm/s (left to right).

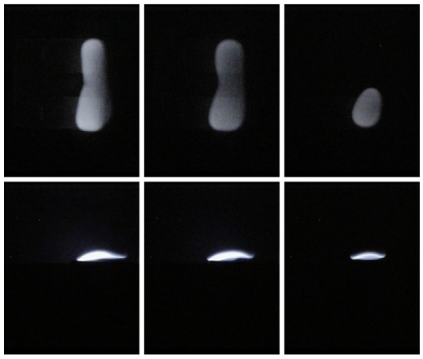

(b) 35% O_2, V_g = 9, 6, and 3 cm/s (left to right).

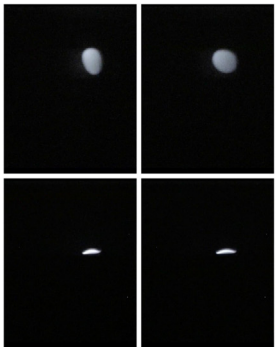

(c) 30% O_2, $V_g = 9$ and 6 cm/s (left to right).

Fig. 3. Flame images illustrating steady-state flame spread at different oxygen concentrations and gas flow velocities. In each graph, upper and lower images correspond to top and side view, respectively. Oxidizing gas flows from left to right and the flames spread against the flow.

The flame spread process at 35%O_2 exhibits a similar trend, except that only one flamelet forms when V_g is reduced from 6 to 3 cm/s. Likewise, the flamelet eventually extinguishes after the gas flow is shut off. When the oxygen concentration is decreased to 30%, one flamelet forms following uniform ignition of the fuel sample at $V_g = 9$ cm/s. Thereafter, it survives the gas flow velocity of 6 cm/s but eventually extinguishes when V_g is further decreased to 3 cm/s. At 25%O_2 (not shown in Fig. 3), the fuel sample was successfully ignited at $V_g = 9$ cm/s, but after the igniter was powered off the resulting flame failed to spread forward and

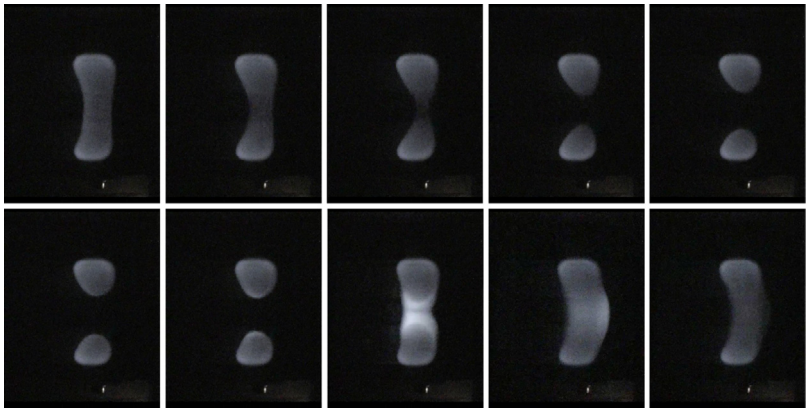

Fig. 4. A sequence of top-view flame images illustrating one cycle of flame oscillation during the transition from $V_g = 6$ to 3 cm/s at 40% O_2. The images, from left to right, top to bottom, correspond to consecutive instants that are separated by an equal time interval $\Delta t = 0.04$ s. Oxidizing gas flows from left to right.

Table 2
Steady-state morphology of upstream spreading diffusion flames at different oxygen concentrations and gas flow velocities.

Oxygen concentration C_a	Gas flow velocity V_g (cm/s)	Flame morphology
40%	9	continuous flame
	6	continuous flame
	3	two flamelets
	0	extinguished
35%	9	continuous flame
	6	continuous flame
	3	one flamelet
	0	extinguished
30%	9	one flamelet
	6	one flamelet
	3	extinguished
	0	extinguished
25%	9	extinguished
	6	extinguished
	3	extinguished
	0	extinguished

eventually extinguished. A summary of the morphological features of the upstream spreading diffusion flames at different oxygen concentrations and gas flow velocities is given in Table 2.

3.1.2. Flame oscillations

At each oxygen concentration, the spreading flame responds to the sudden step change of the gas flow velocity by adjusting its shape, size and spread rate, until eventually re-stabilizing itself at a new steady state after a dynamic transition. This transient stage is relatively short (generally < 10 s) if the transition takes place between two similar flame shapes, e.g., from continuous flame to continuous flame, as in the case from 9 to 6 cm/s at 40% O_2, or from flamelet to flamelet, as in the case from 9 to 6 cm/s at 30% O_2. By contrast, if the transition involves a radical change in the flame shape, e.g., from continuous flame to flamelet, as in the case from 6 to 3 cm/s at 40% O_2, the transient stage lasts much longer (several tens of seconds) and is usually accompanied by flame oscillations.

Figure 4 shows one cycle of flame oscillation at the early stage of the transition from 6 to 3 cm/s at 40% O_2, through a sequence of top-view flame images captured at ten equal-interval instants. It is evident that the flame oscillation is characterized by repeated division and coalescence of the entire diffusion flame along the lateral direction. The oscillation lasts for about 40 s, with the frequency decreasing consistently over time (the frequency at the time corresponding to Fig. 4 is about 2.8 Hz), until the eventual formation of two stabilized flamelets. Similar oscillations were also observed at 35% O_2, during the transition from a continuous flame at $V_g = 6$ cm/s to one single flamelet at 3 cm/s.

The flame oscillations observed during the transition from the continuous flame mode to the flamelet mode may be accounted for by the disparity in the thermal diffusion time scales associated with the gas and the solid phase. Note that the longitudinal thermal diffusion time scales associated with the gas and the solid phase are, respectively, $t_g = L_g^2/\alpha_g$ and $t_s = L_s^2/\alpha_s$, where L_g and L_s are the characteristic longitudinal length scales near the flame leading edge associated with the gas and solid phase, respectively, and α_g and α_s are the corresponding thermal diffusivities. The two length scales L_g and L_s are roughly comparable in most cases [17], whereas the solid thermal diffusivity is in general far smaller than that of the gas. Consequently, $t_g/t_s \sim \alpha_s/\alpha_g \ll 1$, which means that, once the thermal balance is altered due to a sudden change in the gas flow velocity, the solid phase needs a much longer relaxation time than the gas phase to reach a new equilibrium state. Take the 40% O_2 case as an example. In response to the sudden change of the gas flow velocity from 6 to 3 cm/s, the diffusion flame shrinks and splits into two flamelets quickly. The fuel surface between the two flamelets, however, is still hot and continues to release fuel vapor into the oxidizer stream. The resulting combustible mixture is then ignited intermittently by the edge flames that develop at the edge of the flamelets, leading to periodic flame oscillations over the fuel surface between the two flamelets. With consistent cooldown of the fuel surface, the oscillation decays in time and eventually dies out when the middle solid fuel ceases to vaporize.

Oscillations also occur prior to extinction of flamelets following sudden reduction of the gas flow velocity. Figure 5 illustrates the pre-extinction oscillating process of the two flamelets at 40% O_2 when the gas flow is shut off from 3 cm/s. The oscillation lasts only for about 1 s, far shorter than that during the transition from the continuous flame mode to the flamelet mode. The oscillation mechanism, however, can be understood along the same lines.

Similar mechanisms have been proposed for flame oscillations occurring in other contexts, e.g., before local extinction of the trailing edge of spreading diffusion flames over thick PMMA plates [20], and after stagnation region blowoff of diffusion flames around cylindrical PMMA rods in concurrent axial flows [33]. It should be emphasized that thermal interactions between the flames and the solids play a very important role in the flame oscillations encountered in all these circumstances (including the present one), and therefore the underlying mechanisms are substantially different from that behind pulsating flames, for which intrinsic flame instability constitutes the primary cause [34]. It is interesting to note that flame oscillations due to flame/solid thermal interactions have

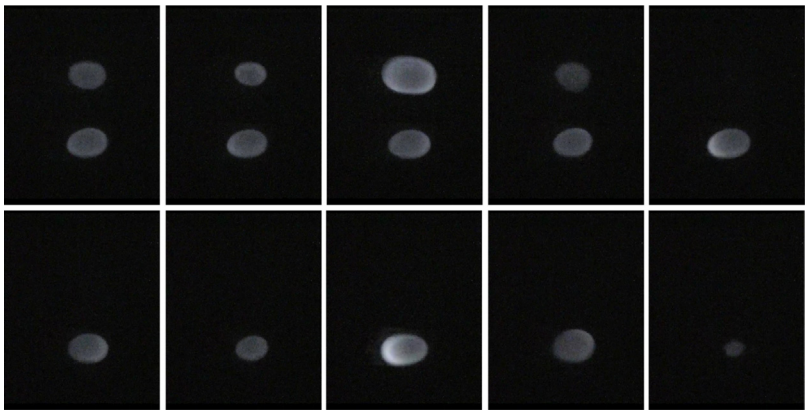

Fig. 5. Top-view flame images illustrating the pre-extinction oscillation of two flamelets during the transition from $V_g = 3$ to 0 cm/s at 40% O_2. The images, from left to right, top to bottom, correspond to consecutive instants that are separated by an equal time interval $\Delta t = 0.08$ s. Oxidizing gas flows from left to right.

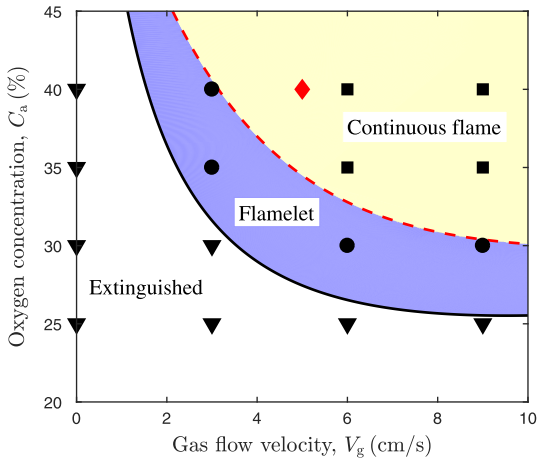

Fig. 6. A flammability map and stability diagram showing the distribution of the continuous flame zone, the flamelet zone, and the extinguished zone on the C_a–V_g plane. The solid and dashed lines correspond to the flammability boundary and the marginal stability boundary, respectively. The filled symbols correspond to the steady states listed in Table 2, except for the diamond symbol in the continuous flame zone, which corresponds to the lowest gas flow velocity chosen in the experiment of Vietoris et al. [20].

been observed for premixed flames as well in meso-scale circular tubes [35,36]. These oscillations share similar mechanisms and features with those mentioned above within the flame spread context, except for two major differences—in the context of the tubular flames the tube wall is inert and therefore neither vaporizes nor participates in the chemical reactions; in addition, a limit cycle is eventually formed, corresponding to sustained flame oscillations.

3.2. Flammability map and stability diagram

The final steady states of flame spread at different oxygen concentrations and gas flow velocities, which are summarized in Table 2, can be visualized by the flammability map shown in Fig. 6. As can be seen, a flammability boundary divides the entire C_a–V_g plane into two zones, namely a flammable zone and a non-flammable, or extinguished zone, corresponding to parameter spaces where sustained flame spread can and cannot exist, respectively. Within the flammable zone, there exists another boundary, which separates a continuous flame sub-zone, where the leading edge of the spreading diffusion flames is continuous along the transverse direction, from a flamelet sub-zone where the diffusion flames take the form of transversely distributed, isolated flamelets. Note that the two boundaries are approximately determined according to neighboring discrete data points, so the associated errors are within 5% in oxygen concentration and 3 cm/s in gas flow velocity.

The flammability map shown in Fig. 6 may also be viewed as a diagram illustrating the stability properties of the spreading flames, with C_a and V_g as two independent control parameters. In the continuous flame zone, although the leading diffusion flame front generally has nonuniform spread rates because of the side oxygen diffusion effects, the shape of the flame front remains essentially unchanged at fixed oxygen concentrations and gas flow velocities, and therefore the flame front is regarded to be stable. By contrast, within the flamelet zone continuous flames are no longer stable, and the flamelets are considered to be the consequent steady structure developed after the onset of instability. In this sense, the boundary that separates the continuous flame zone and the flamelet zone also constitutes the marginal stability boundary.

The instability identified above occurs exclusively near the quenching limit, where radiative heat loss plays an important role. This scenario is reminiscent of the fingering instability of flame or smolder spread over thin solid fuels [37–41], as well as the cellular instability of gaseous-fuel diffusion flames near the quenching limit [42], both of which have been argued to have a diffusive-thermal origin. As mentioned in the Introduction, for opposed-flow flame spread over thick PMMA plates, the formation of flamelets has been observed by Matsuoka et al. [23] in a normal-gravity experiment. The identification of a similar flamelet spread mode in the present microgravity experiment, which excludes the complexity of buoyancy effects, justifies the diffusive-thermal nature of the instability associated with the formation of flamelets in both experiments. Despite the difference in the reaction modes, so far as stability of the reaction fronts is concerned, flame spread and smolder front propagation share many common features and the essential physical mechanisms underlying the displayed instabilities are in general very similar [43]. Analysis shows that, for near-quenching-limit opposed-flow smolder spread over thin solid fuels, the characteristic width of the fingers developed after the onset of instability is correlated with the heat loss intensity, whereas the characteristic separation distance between neighboring fingers is correlated with the Peclet number of the gas flow [44]. It is expected that similar correlations may equally apply to the characterization of the flamelets identified in the present experiment. Its verification, however, entails more comprehensive data from the flamelet zone and thus calls for further experimental or numerical efforts.

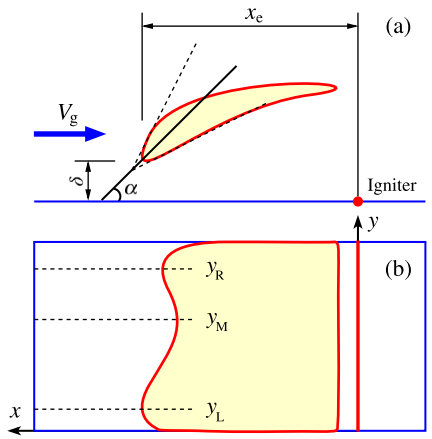

Fig. 7. Schematics illustrating the determination of the three characteristic parameters associated with the flame leading edge. (a) side view and (b) top view.

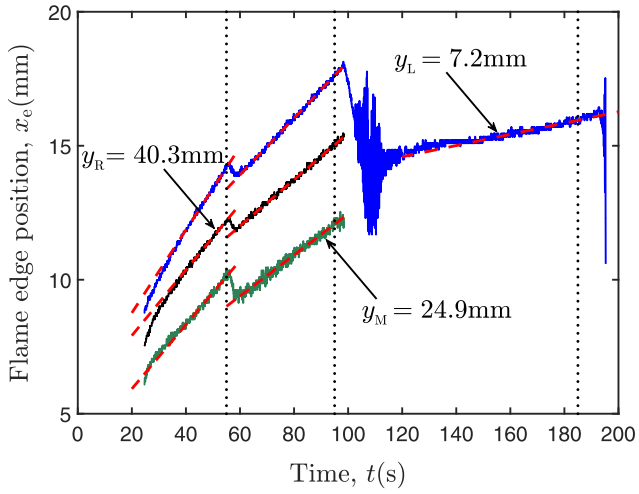

Fig. 8. Time evolution of the flame leading edge position x_e corresponding to three representative y locations at oxygen concentration $C_a = 35\%$. Dotted lines mark the instants when a step change of the gas flow velocity is implemented (see Table 1), and dashed lines correspond to piecewise linear fitting of the time evolution curves of x_e.

3.3. Characteristic parameters describing the flame spread

The top- and side-view videos recorded by the CCD cameras were analyzed frame by frame in an effort to quantify the flame spread processes. Attention is primarily focused on the flame leading edge, where heat conduction from the flame to the solid serves as the main driving force of flame spread in the opposed-flow configuration. As schematically illustrated in Fig. 7, associated with the flame leading edge three parameters may be extracted to characterize the structural and dynamical properties of the spreading diffusion flame, namely the standoff distance of the flame leading edge away from the fuel surface, δ, the spread rate of the flame, V_f, which can be determined according to the time evolution of the flame leading edge position relative to the igniter, x_e, and the flame inclination angle, α, which is defined as the angle between the fuel surface and the bisector of the angle formed by the two external tangents of the flame profile near the leading edge. Among these parameters, δ and α are determined according to the side-view flame images, whereas V_f is determined according to the top-view images. In identifying the boundary of the flame, the same pixel threshold has been used for each oxygen concentration.

3.3.1. Flame spread rate

As mentioned in the Introduction, we adopted a relatively wide fuel sample in the present experiment and expected that the overall effects of side oxygen diffusion could be significantly reduced. The price of using a wide fuel, however, is that at low flow velocities the leading edge of a continuous flame generally develops a non-uniform shape, thus bringing about the problem of nonuniqueness of the leading edge position and the associated flame spread rate. To provide a more balanced view of the spreading flames, for the continuous flame mode we choose three representative locations along the transverse direction, namely y_L, y_M and y_R, to track the position of the flame leading edge. As shown in Fig. 7(b), y_L and y_R, which correspond to the two convex apexes of the flame leading edge, are close to the two sides of the fuel sample and thus the spread of the local flame fronts is favored by the side oxygen diffusion effects; by contrast, the local flame front at y_M, which corresponds to the concave bottom of the flame leading edge, is least influenced by the side oxygen diffusion effects and thus lags behind the two side ones. For flame spread in the flamelet mode, the flame leading edge position x_e is simply identified with the leading point of each flamelet.

Figure 8 shows the time evolution of the flame leading edge position x_e at three representative y locations for the 35% O_2 case. At each y location, for each gas flow velocity the flame front tends to a steadily propagating state after a transient due to ignition or transition between different gas flow velocities, and thus a local spread rate V_f can be determined by linearly fitting the time evolution curve of x_e. The local flame spread rates determined in this way at different oxygen concentrations and gas flow velocities are listed in Table 3. It is evident that, at each oxygen concentration, the local flame spread rate at each y location tends to decrease with decreasing gas flow velocity. On the other hand, at each fixed gas flow velocity, with few exceptions (due to lateral flame nonuniformities) the flame spread rate at each y location shows a tendency to decrease with decreasing oxygen concentration.

To facilitate the comparison between different oxygen concentrations and gas flow velocities, we introduce a mean flame spread rate $\overline{V}_f$, which is defined as the average of the left flame spread rate $V_{f,L}$ and the right flame spread rate $V_{f,R}$ for continuous flames or double flamelets, whereas for single flamelets it is simply taken as the spread rate of the flamelets. In Table 3, the corresponding mean flame spread rates are listed in the rightmost column.

For opposed-flow flame spread over thick solid fuels, to get an overall picture of the dependence of the flame spread rate on the gas flow velocity over the full range, we combine the present experimental data with some currently available experimental results and plot in Fig. 9 the normalized flame spread rate, $V_f/V_{f,EST}$, as a function of the global Damköhler number Da, which is inversely related to the gas flow velocity V_g. Here $V_{f,EST}$ is predicted by the extended simplified theory (EST) of Bhattacharjee et al. [14], and the definition of Da follows Fernandez-Pello et al. [15]. All the three sets of data presented in Fig. 9 are for thick PMMA. The data of Fernandez-Pello et al. [15] cover the high and intermediate range of the gas flow velocity and therefore correspond to the kinetics-controlled and thermal regimes of opposed-flow flame spread. The data of Zhu et al. [22], which were obtained in a narrow-channel flame spread experiment, correspond to the transition from the thermal regime toward the radiation-controlled regime. The data of the present microgravity experiment, which are based on the mean flame spread rate defined above, lie in the lowest range of the gas flow velocity, and therefore fall completely within the radiation-controlled regime.

Despite the comparatively larger scatter of the present experimental data, which may be partly attributed to the uncertainties induced by the introduction of the mean flame spread rate,

Table 3
Local flame spread rates at three representative y locations and the mean flame spread rate under different oxygen concentrations and gas flow velocities. The three y locations vary slightly with different oxygen concentrations but remain unchanged at each oxygen concentration. '—' stands for 'not applicable'.

Oxygen concentration C_a	Gas flow velocity V_g (cm/s)	Left flame spread rate $V_{f,L}$ (mm/s)	Middle flame spread rate $V_{f,M}$ (mm/s)	Right flame spread rate $V_{f,R}$ (mm/s)	Mean flame spread rate $\overline{V}_f$ (mm/s)
40%	9	0.150	0.148	0.158	0.154
	6	0.099	0.057	0.106	0.102
	3	0.040	—	0.039	0.040
35%	9	0.155	0.120	0.123	0.139
	6	0.106	0.077	0.087	0.096
	3	0.021	—	—	0.021
30%	9	—	0.028	—	0.028
	6	—	0.018	—	0.018

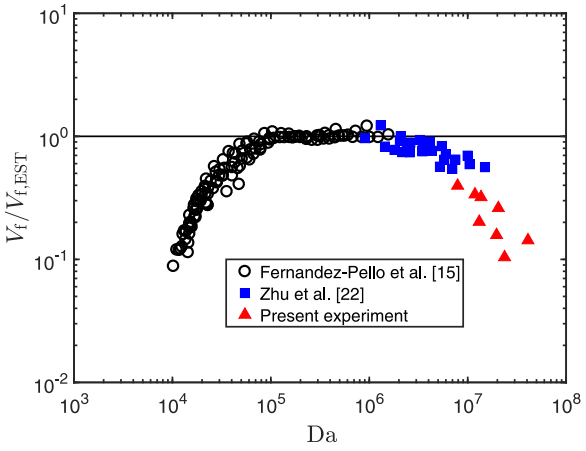

Fig. 9. The dependence of the normalized flame spread rate $V_f/V_{f,EST}$ on the global Damköhler number Da.

the normalized flame spread rate displays an apparent inverse U-shaped dependence upon the global Damköhler number Da. Specifically, at intermediate Damköhler numbers, the flame spread is dominated by the heat transfer mechanism and thus V_f is well predicted by the extended simplified theory of Bhattacharjee et al. [14], which applies specifically to the thermal regime. The decline of $V_f/V_{f,EST}$ at small and large Damköhler numbers results from the finite kinetics effects and the radiative heat loss effects, respectively, as implied by the names of the two regimes. Note that besides the global Damköhler number Da, a local Damköhler number or a local mass transfer number, as defined by Chen and T'ien [45] and Torero et al. [6], may be introduced to characterize the local burning state at the leading flame front. The spread rate of the leading flame front may then be expressed as a function of the local Damköhler number or local mass transfer number. As a result, the decline of the flame spread rate at the two opposite extremes of the global Damköhler number may be universally accounted for by the decrease in the *local* Damköhler number or *local* mass transfer number. We note that a similar local Damköhler number has been introduced by Lu and Matalon [46] to be associated with the propagation velocity of edge flames in growing mixing layers.

3.3.2. Standoff distance and inclination angle at the flame leading edge

Figure 10 shows the time evolution of the leading edge flame standoff distance δ and the leading edge flame inclination angle α at 35% O_2. It is evident that, at each gas flow velocity both δ and α tend to constant values after the transient decays. Another clear tendency manifested by the data is that the flame standoff distance increases while the flame inclination angle decreases with the decrease in the gas flow velocity. In other words, the spreading

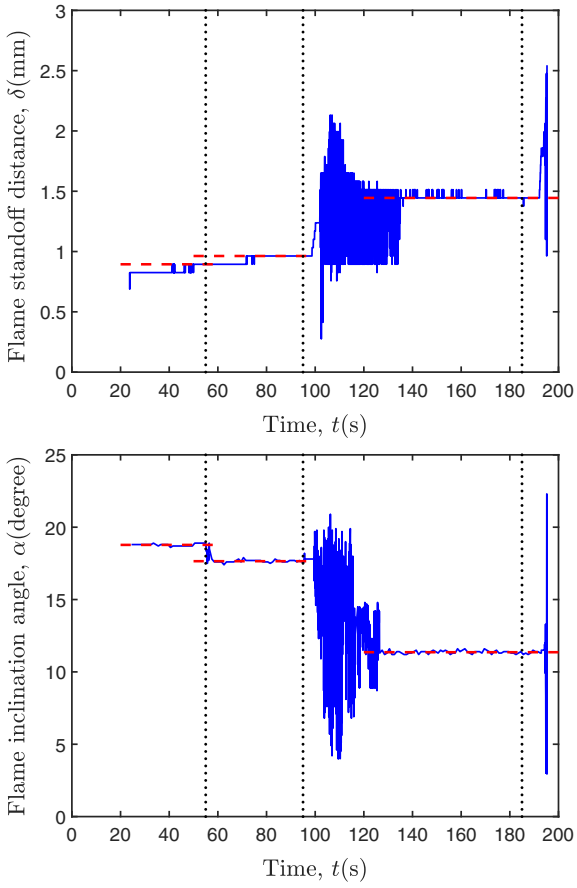

Fig. 10. Time evolution of the leading edge flame standoff distance δ and the leading edge flame inclination angle α at 35% O_2. Dotted lines mark the instants when a step change of the gas flow velocity is implemented (see Table 1), and dashed lines correspond to piecewise fitting of the data with constants.

diffusion flame stands farther from the surface of the solid fuel and meanwhile becomes more flattened in response to the reduction of the gas flow velocity. In addition, note that besides x_e (see Fig. 8), both δ and α display oscillations during the transition process from the continuous flame mode toward the flamelet mode as well as before extinction. This suggests that the flame oscillations are essentially three-dimensional global behavior of the diffusion flames. Table 4 lists the values of δ and α at different oxygen concentrations and gas flow velocities. The flame standoff distance data for 30% O_2 are not available because of excessively large uncertainties encountered in that case when trying to identify the flame boundary from the flame images.

Table 4
Values of the leading edge flame standoff distance δ and the leading edge flame inclination angle α at different oxygen concentrations and gas flow velocities. 'N/A' stands for 'not available'.

Oxygen concentration C_a	Gas flow velocity V_g (cm/s)	Flame standoff distance δ (mm)	Flame inclination angle α (degree)
40%	9	0.42	22.7
	6	0.51	19.8
	3	0.92	15.4
35%	9	0.89	18.8
	6	0.96	17.7
	3	1.44	11.4
30%	9	N/A	17.4
	6	N/A	15.9

It is postulated that the flame standoff distance, the flame inclination angle, and the flame spread rate are inter-correlated among different oxygen concentrations and gas flow velocities. To test this postulation, we show in Fig. 11 plots of δ and α against $\overline{V}_f$ using the data given in Tables 3 and 4. As can be seen, among different oxygen concentrations there is a somewhat large scatter of the data, especially the flame standoff distance, which is extremely small and thus its measurement through flame image processing would be subject to serious uncertainties. Nevertheless, a clear tendency may be identified from the limited data shown in Fig. 11: the more slowly the diffusion flame spreads, the farther the flame leading edge stands away from the surface of the solid fuel, and the more flattened the flame becomes. This is consistent with the variations of δ and α with respect to the gas flow velocity V_g, since the flame spread rate is positively correlated with the gas flow velocity for the currently considered low-velocity regime.

3.4. Surface energy balance analysis

Forward heat transfer from the flame to the solid in the vicinity of the flame leading edge is considered to be one of the main controlling mechanisms of opposed-flow flame spread [8–10]. To gain insight into the mechanisms underlying the transition between different spreading modes as well as flame extinction, we proceed to carry out a surface energy balance analysis near the flame leading edge.

Consider a unit area on the gas/solid interface beneath the flame leading edge. Heat input through this area from the flame has two origins, namely gas phase heat conduction and radiative heat transfer. As suggested by Olson et al. [21], under near-limit conditions as considered in the present study, radiative heat transfer is negligible and hence forward heat transfer from the flame to the solid is dominated by gas phase heat conduction. Among the total amount of heat conducted to the solid, one portion is dissipated to the ambient environment through surface radiation, another portion is absorbed by the solid fuel as the source of heat for vaporization, and the rest portion is transferred to the interior of the solid by conduction. To summarize, across the gas/solid interface beneath the flame leading edge, the following surface energy balance relation holds:

$$\underbrace{\lambda_g \frac{\partial T_g}{\partial y}}_{q_{GPC}} = \underbrace{\lambda_s \frac{\partial T_s}{\partial y}}_{q_{SPC}} + \underbrace{\dot{m} L_v}_{q_{VAP}} + \underbrace{\varepsilon \sigma \left(T_s^4 - T_\infty^4\right)}_{q_{RAD}}, \tag{1}$$

where, from left to right, the four terms represent, respectively, the gas and the solid phase conductive heat flux normal to the phase interface, the heat absorbed by the solid for vaporization, and the surface radiative heat loss. T_g and T_s represent, respectively, the gas and the solid temperature, λ_g and λ_s are, respectively, the heat conductivity of the gas and the solid phase, $\dot{m}$ is the mass burning rate, L_v is the latent heat of vaporization, ε is the radiative emittance, σ is the Stefan–Boltzmann constant, and T_∞ is the ambient temperature.

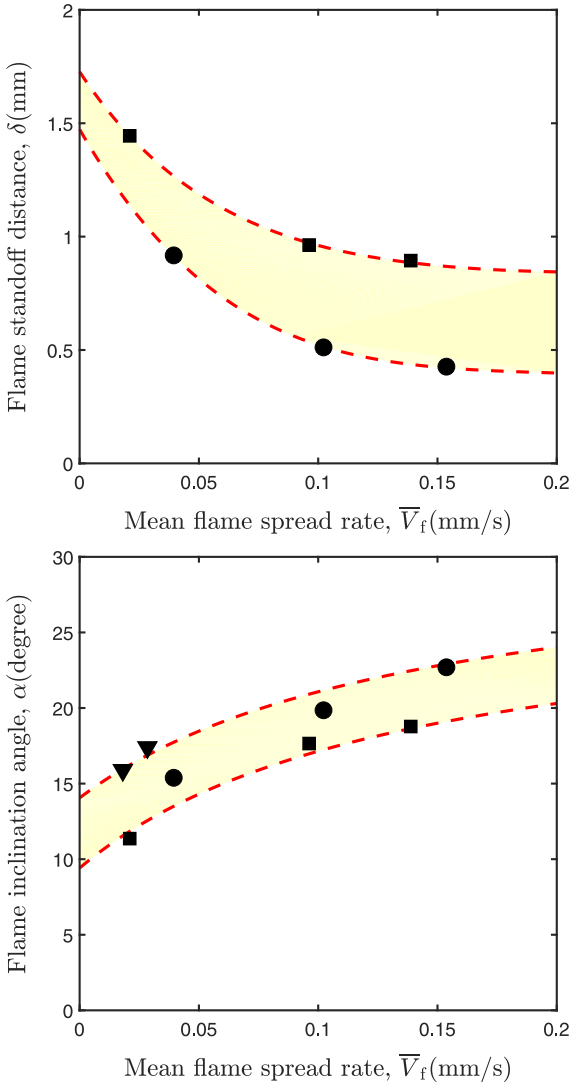

Fig. 11. The dependence of the leading edge flame standoff distance δ and the leading edge flame inclination angle α on the mean flame spread rate $\overline{V}_f$ at different oxygen concentrations and gas flow velocities. The black-filled circle, square, and triangle symbols correspond to data from Tables 3 and 4 at oxygen concentrations $C_a = 40\%$, 35% and 30%, respectively.

The gas temperature field near the flame leading edge needs to be resolved to evaluate the gas conductive heat flux term in Eq. (1). Figure 12 shows the time history of gas and fuel surface temperatures at 40% O_2, measured by the five thermocouples T_1–T_5 as shown in Fig. 2. For thermocouple T_1, which was positioned 1 mm above the fuel surface along the streamwise centerline and 8 mm away from the ignition wire, following an initial transient after ignition, at $t = 45$ s the temperature peaks at about 692 K. Next, with the gas flow velocity reduced to 6 cm/s, the temperature drops gradually from 660 K to 648 K. Then, shortly after the gas flow velocity is further reduced to 3 cm/s, the temperature displays oscillations, which apparently correspond to the flamelet formation stage illustrated in Fig. 4. Subsequently, with the stabilization of the resulting two isolated flamelets, the temperature drops consistently with time until the final extinction of the flamelets. Such temperature values measured by T_1, which are considerably lower than typical temperatures of diffusion flames, imply that

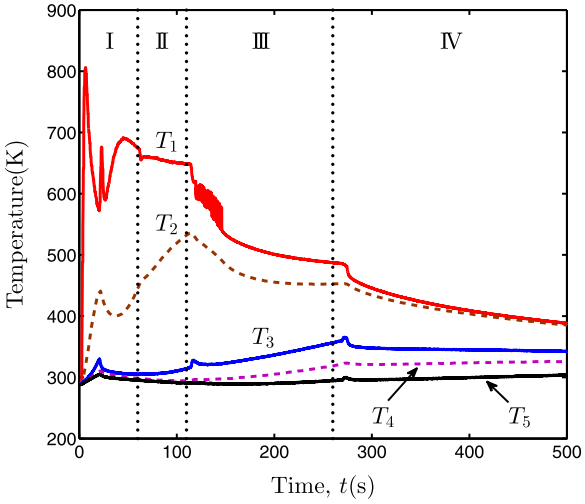

Fig. 12. Time history of temperature measured by the five thermocouples T_1–T_5 (see Fig. 2 for their positioning details) at 40% O_2. I–IV mark the time intervals corresponding to the four gas flow velocities (see Table 1).

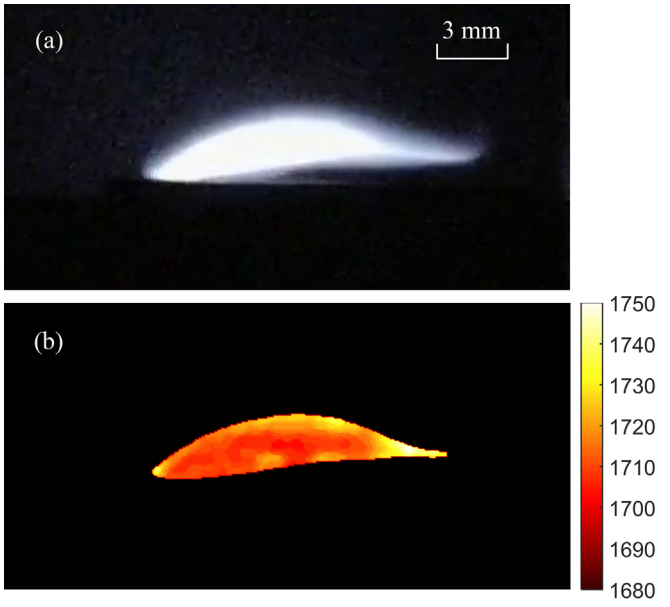

Fig. 13. Reconstructed temperature field of the spreading diffusion flame according to the RGB two-color pyrometry method. (a) A side-view flame image taken at 35% O_2, under gas flow velocity $V_g = 9$ cm/s; (b) the corresponding reconstructed temperature contours. Temperature unit: K.

during the whole flame spread process the thermocouple has not been swept by the core region of the flame, and thus has failed to capture the flame temperature at the leading edge.

The reason for the failure differs depending on the stage of the flame spread process. Specifically, in the continuous flame stage, although the flame position data indicate that the leading flame front has passed the thermocouple T_1, the middle segment of the flame front, which had a relatively lower oxygen concentration than the two sides, might stand so high above the fuel surface that the flame temperature was not sensed by the thermocouple below. By contrast, in the flamelet stage, the two flamelets distributed symmetrically with respect to the streamwise centerline, and thus have not passed the thermocouple at all. The remaining thermocouples T_3 and T_5, which were also placed along the centerline for gas-phase temperature measurement, and were even farther away from the ignition wire than T_1, also failed to capture the flame temperature either before or after the formation of the flamelets. Similar problems exist as well in other two oxygen concentration cases. Consequently, it is essentially not feasible to calculate the gas conductive heat flux term in Eq. (1) based on the temperature data measured by the thermocouples.

In the following analysis we resort to an alternative method, the RGB two-color pyrometry method, to resolve the temperature field of the diffusion flames. As a kind of non-intrusive temperature measurement technique, the RGB two-color pyrometry method has found extensive applications in various combustion problems, e.g., the determination of the radiative temperature of burning solid particles (including both soot and single coal particles) [47–49], the measurement of the temperature field of diffusion flames [50–52], and the determination of the temperature of solid surfaces with varying emissivities [53]. For details regarding the underlying mechanisms of the method and the involved reconstruction technique, the readers are referred to Refs. [51,53].

Figure 13 exemplifies the temperature field reconstructed by the two-color pyrometry method according to a side-view image taken at 35% O_2, for gas flow velocity $V_g = 9$ cm/s. The reconstruction algorithm has been calibrated by comparison with reference temperatures measured with a thermocouple in a 1g flame spread experiment using the same experimental setup. In the following surface energy balance analysis, we will use the flame leading edge temperature determined according to this method to calculate the gas phase conductive heat flux.

Table 5
Parameter values used in the calculation of Eq. (1). The values corresponding to the gas phase are chosen at a reference temperature $T_{ref} = 600$ K.

Parameters	Parameter values	Units
λ_g	4.60×10^{-4}	W/cm/K
λ_s	1.88×10^{-3}	W/cm/K
ρ_g	5.76×10^{-4}	g/cm^3
ρ_s	1.19	g/cm^3
c_p	1.054	J/g/K
c_s	1.465	J/g/K
T_v	618	K
T_∞	285	K
ε	0.85	
σ	5.67×10^{-12}	W/cm^2/K^4

The gas phase conductive heat flux term in Eq. (1) is approximated by a linear difference relation, i.e., $q_{GPC} = \lambda_g \partial T_g/\partial y \approx \lambda_g (T_f - T_v)/\delta$, where T_f and T_v represent, respectively, the temperature at the flame leading edge and the vaporization temperature of the solid fuel. Likewise, the solid phase conductive heat flux is approximated as $q_{SPC} = \lambda_s \partial T_s/\partial y \approx \lambda_s (T_v - T_\infty)/\delta_s$, where $\delta_s = (\alpha_s t_h)^{1/2}$ represents the depth of the heated fuel layer beneath the flame leading edge, with $t_h = \alpha_g / V_g \bar{V}_f$ the heating time [17]. The surface radiative heat loss term $q_{RAD} = \varepsilon\sigma(T_s^4 - T_\infty^4)$ is calculated with the solid temperature T_s replaced by the solid fuel vaporization temperature T_v. Then, according to the energy balance relation (1), the heat absorption term q_{VAP} is determined by subtracting the two heat loss terms from the gas phase conductive heat flux, i.e., $q_{VAP} = \dot{m} L_v = q_{GPC} - q_{SPC} - q_{RAD}$.

Table 5 lists the parameter values used in the calculation of Eq. (1), and Table 6 lists the values of each term calculated for different gas flow velocities at 35% and 40% O_2. The values for 30% O_2 are not shown because the flame standoff distance data for that case are not available. The apparently unphysical values of q_{VAP} obtained at 35% O_2 for $V_g = 9$ and 6 cm/s may be attributed to the uncertainties associated with the flame standoff distance, which result in an underestimate of the q_{GPC} values.

Table 6
Values of the four terms in Eq. (1) evaluated under different gas flow velocities at 35% and 40% O_2. The '*' symbol marks unphysical values due to errors introduced in the measurement of the flame standoff distance.

Oxygen concentration C_a	Gas flow velocity V_g (cm/s)	q_{GPC} (W/cm^2)	q_{SPC} (W/cm^2)	q_{VAP} (W/cm^2)	q_{RAD} (W/cm^2)
40%	9	12.51	8.08	3.76	0.67
	6	10.24	5.38	4.19	0.67
	3	5.66	2.37	2.62	0.67
35%	9	5.77	7.67	−2.57*	0.67
	6	5.21	5.21	−0.67*	0.67
	3	3.46	1.72	1.07	0.67

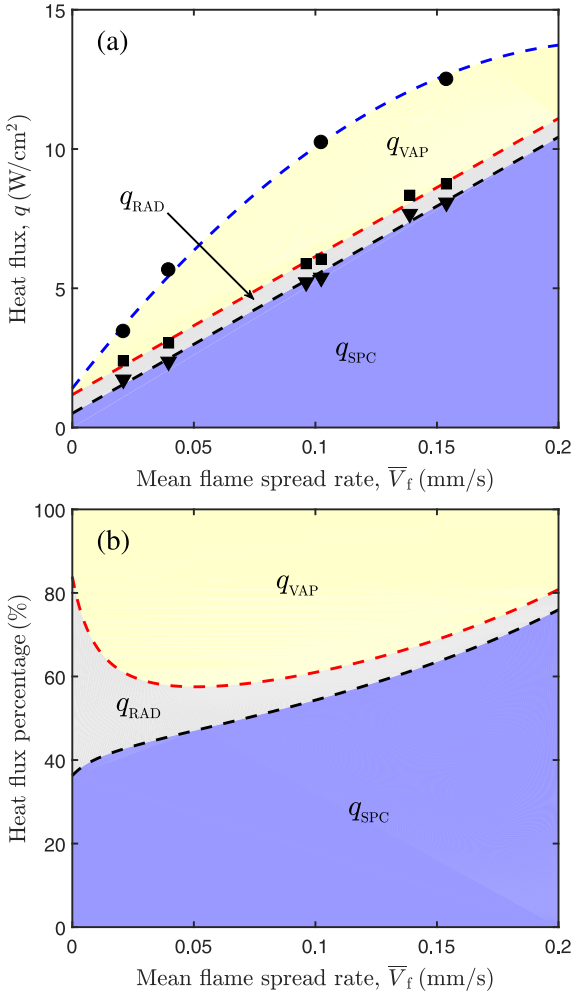

Fig. 14. Heat fluxes in the surface energy balance equation (1) and their percentages out of the total energy input as a function of the mean flame spread rate $\overline{V}_f$. Black-filled circle, triangle and square symbols correspond, respectively, to the values of q_{GPC}, q_{SPC}, and $q_{SPC}+q_{RAD}$ as listed in Table 6. The unphysical values marked by the '*' symbol in Table 6 are not shown.

Figure 14(a) plots the heat flux terms listed in Table 6 against the mean flame spread rate $\overline{V}_f$. In addition, the percentage of each heat flux on the right hand side of Eq. (1) out of the total heat input q_{GPC} is plotted against $\overline{V}_f$ in Fig. 14(b). It is evident that, for the near-limit spreading flames considered in the present study, the surface radiative heat loss q_{RAD} remains essentially unchanged with $\overline{V}_f$, whereas q_{SPC}, the conductive loss to the fuel bed, grows almost linearly with $\overline{V}_f$. By contrast, the total energy input through gas phase conduction, q_{GPC}, exhibits a sub-linear trend with $\overline{V}_f$. As a result, the variation of the heat absorbed by the solid fuel for vaporization, q_{VAP}, and hence the mass burning rate $\dot{m}$, is also sub-linear with respect to $\overline{V}_f$. This implies that the regression depth of the solid fuel, which relates to the mass burning rate and the flame spread rate as $h \sim \dot{m}/\overline{V}_f$, tends to increase with decreasing flame spread rate. The verification of this inference, however, has not been possible in the present microgravity experiment because the test fuel samples were not recovered.

Figure 14(b) indicates that the percentages of the two heat losses have opposite trends with the change in the flame spread rate: the percentage of the conductive heat losses to the fuel bed decreases approximately linearly with decreasing flame spread rate, whereas that of the radiative losses increases monotonically with the decrease in $\overline{V}_f$, and moreover, the rate of increase accelerates drastically as $\overline{V}_f$ approaches the vanishing limit. As a consequence, the percentage of the overall heat losses undergoes a rapid growth with the approach of vanishing spread rate, until the extinction of the entire flame at a certain quenching limit. Recall that in the flammability map shown in Fig. 6, the quenching boundary is identified according to two environment parameters, namely the oxygen concentration and the gas flow velocity. The current surface energy balance analysis, however, seems to support the view that flame quenching is intrinsically associated with a limiting ratio of the overall heat losses, or equivalently, a limiting flame spread rate, both of which assume certain specific values that are independent of the external oxygen concentration and flow conditions. The finite discrete values chosen for the environment parameters in the present experiment preclude precise determination of the quenching heat loss ratio and the associated flame spread rate. As an estimate, we note that, as displayed by Fig. 14(b), near the vanishing spread rate limit the radiative heat losses are comparable to the conductive losses to the fuel bed, and the overall heat losses amount to about 80% of the total heat input from the flame, a percentage that is in quantitative agreement with the estimates of Olson et al. [21] and Armstrong et al. [54]. Along the same lines, it is further postulated that the marginal stability boundary delineated in Fig. 6 may also be associated with a critical ratio of the overall heat losses and a critical flame spread rate.

4. Conclusions

A microgravity experiment has been performed, in an effort to elucidate the structural and dynamical characteristics of opposed-flow flame spread over thick solid fuels in the low-velocity radiation-controlled regime. A 50-mm wide PMMA sample was adopted as the solid fuel, and for each of the four oxygen concentration cases considered, four decrementally changing gas flow velocities were imposed such that a wide range of parameter values were spanned near the quenching limit. Conclusions are drawn as follows.

(1) Two distinct flame spread modes were identified, namely the continuous flame mode, characterized by flames with a continuous leading front that extends across the sample width and

spreads at essentially uniform speeds (excluding the side diffusion effects of oxygen), and the flamelet mode, characterized by flames taking the form of isolated egg-shaped flamelets that distribute along the transverse direction. At a given oxygen concentration, the continuous flame and flamelet modes develop at high and low flow velocities, respectively, and the transition between these two spread modes due to decrementally changing gas flow velocities is usually accompanied by flame oscillations, the mechanism of which may be accounted for by the disparity in the thermal diffusion time scales associated with the gas and the solid phase. Similar mechanism may also account for flame oscillations occurring prior to flame extinction.

(2) A flammability map around the quenching boundary was delineated, with the oxygen concentration and the gas flow velocity as two control parameters. Further, within the flammable zone, a marginal stability boundary was identified, which separates a stable flame spread sub-zone characterized by the continuous flame mode, from an unstable sub-zone where continuous flames are unstable and steady isolated flamelets result after the onset of instability. Diffusive-thermal instability of the leading flame front was identified as the mechanism controlling the transition between the two spread modes.

(3) A correlation analysis of the experimental data among different oxygen concentration levels indicated that the normalized flame spread rate exhibits an apparent decreasing trend with the flame Damköhler number within the presently considered radiation-controlled regime. Meanwhile, with the decrease in the flame spread rate, the standoff distance and the inclination angle at the flame leading edge show an increasing and decreasing trend, respectively. In other words, the more slowly the flame spreads, the farther the flame stands away from the fuel surface, and the more flattened the flame becomes.

(4) According to an energy balance analysis across the fuel surface beneath the flame leading edge, the variation of the heat absorbed by the solid for vaporization is sub-linear with respect to the flame spread rate, implying that the fuel regression depth has a tendency to increase with decreasing flame spread rate. Moreover, with the approach of the vanishing spread rate limit, the proportion of the overall heat losses (i.e., the surface radiative heat losses plus the conductive losses to the fuel bed) among the total heat conducted from the flame undergoes a rapid growth, until the final extinction of the entire flame at a certain quenching limit. It is postulated that, on the flammability map, the quenching boundary and the marginal stability boundary are, respectively, intrinsically associated with a limiting and a critical ratio of the overall heat losses, or equivalently, associated with a limiting and a critical flame spread rate.

Acknowledgments

This work is supported by the National Natural Science Foundation of China, under grant No. U1738117, and by the Strategic Priority Research Program on Space Science, the Chinese Academy of Sciences, under grant Nos. XDA04020410 and XDA04020202-10. The authors would like to thank Jingsong Yang, Renhao Liu, and Liu Tian for their excellent work in development and testing of the flight hardware.

References

[1] F.A. Williams, Mechanisms of fire spread, Symp. (Int.) Combust. 16 (1977) 1281–1294.
[2] NASA-STD-6001B, Flammability, offgassing, and compatibility requirements and test procedures, 2011.
[3] O. Fujita, Solid combustion research in microgravity as a basis of fire safety in space, Proc. Combust. Inst. 35 (2015) 2487–2502.
[4] H.W. Emmons, The film combustion of liquid fuel, Z. Angew. Math. Mech. 36 (1956) 60–71.
[5] P.J. Pagni, T.M. Shih, Excess pyrolyzate, Symp. (Int.) Combust. 16 (1977) 1329–1343.
[6] J.L. Torero, T. Vietoris, G. Legros, P. Joulain, Estimation of a total mass transfer number from the standoff distance of a spreading flame, Combust. Sci. Technol. 174 (2002) 187–203.
[7] A.S. Rangwala, S.G. Buckley, J.L. Torero, Analysis of the constant B-number assumption while modeling flame spread, Combust. Flame 152 (2008) 401–414.
[8] J.N. de Ris, Spread of a laminar diffusion flame, Symp. (Int.) Combust. 12 (1969) 241–252.
[9] A.C. Fernandez-Pello, T. Hirano, Controlling mechanisms of flame spread, Combust. Sci. Technol. 32 (1983) 1–31.
[10] I.S. Wichman, Theory of opposed-flow flame spread, Prog. Energy Combust. Sci. 18 (1992) 553–593.
[11] J.S. T'ien, H.Y. Shih, C.B. Jiang, H.D. Ross, F.J. Miller, A.C. Fernandez-Pello, J.L. Torero, D. Walther, Mechanisms of flame spread and smolder wave propagation, in: H.D. Ross (Ed.), Microgravity Combustion: Fire in Free Fall, Academic Press (2001), pp. 299–418.
[12] I.S. Wichman, F.A. Williams, A simplified model of flame spread in an opposed flow along a flat surface of a semi-infinite solid, Combust. Sci. Technol. 32 (1983) 91–123.
[13] S. Bhattacharjee, J. West, S. Dockter, A simplified theory for de Ris flame over thick and thin fuel beds, Combust. Flame 104 (1996a) 66–80.
[14] S. Bhattacharjee, J. West, R.A. Altenkirch, Determination of the spread rate in opposed-flow flame spread over thick solid fuels in the thermal regime, Symp. (Int.) Combust. 26 (1996b) 1477–1485.
[15] A.C. Fernandez-Pello, S.R. Ray, I. Glassman, Flame spread in an opposed forced flow: the effect of ambient oxygen concentration, Symp. (Int.) Combust. 18 (1981) 579–589.
[16] C. di Blasi, Predictions of wind-opposed flame spread rates and energy feedback analysis for charring solids in a microgravity environment, Combust. Flame 100 (1995) 332–340.
[17] S. Bhattacharjee, R. Ayala, K. Wakai, S. Takahashi, Opposed-flow flame spread in microgravity—theoretical prediction of spread rate and flammability map, Proc. Combust. Inst. 30 (2005) 2279–2286.
[18] J. West, L. Tang, R.A. Altenkirch, S. Bhattacharjee, K. Sacksteder, Quiescent flame spread over thick fuels in microgravity, Symp. (Int.) Combust. 26 (1996) 1335–1343.
[19] R.A. Altenkirch, L. Tang, K. Sacksteder, S. Bhattacharjee, M.A. Delichatsios, Inherently unsteady flame spread to extinction over thick fuels in microgravity, Symp. (Int.) Combust. 27 (1998) 2515–2524.
[20] T. Vietoris, J.L. Ellzey, P. Joulain, S.N. Mehta, J.L. Torero, Laminar diffusion flame in microgravity: the results of the MINITEXUS 6 sounding rocket experiment, Proc. Combust. Inst. 28 (2000) 2883–2889.
[21] S.L. Olson, U. Hegde, S. Bhattacharjee, J.L. Deering, L. Tang, R.A. Altenkirch, Sounding rocket microgravity experiments elucidating diffusive and radiative transport effects on flame spread over thermally thick solids, Combust. Sci. Technol. 176 (2004) 557–584.
[22] F. Zhu, Z. Lu, S. Wang, Flame spread and extinction over a thick solid fuel in low-velocity opposed and concurrent flows, Microgravity Sci. Technol. 28 (2016) 87–94.
[23] T. Matsuoka, K. Nakashima, Y. Nakamura, S. Noda, Appearance of flamelets spreading over thermally thick fuel, Proc. Combust. Inst. 36 (2017) 3019–3026.
[24] S. Link, X. Huang, C. Fernandez-Pello, S. Olson, P. Ferkul, The effect of gravity on flame spread over PMMA cylinders, Sci. Rep. 8 (2018) 120.
[25] M. Thomsen, C. Fernandez-Pello, G.A. Ruff, D.L. Urban, Buoyancy effects on concurrent flame spread over thick PMMA, Combust. Flame 199 (2019) 279–291.
[26] D.L. Urban, P. Ferkul, S. Olson, G.A. Ruff, J. Easton, J.S. T'ien, Y.-T. T. Liao, C. Li, C. Fernandez-Pello, J.L. Torero, G. Legros, C. Eigenbrod, N. Smirnov, O. Fujita, S. Rouvreau, B. Toth, G. Jomaas, Flame spread: effects of microgravity and scale, Combust. Flame 199 (2019) 168–182.
[27] W.E. Mell, T. Kashiwagi, Dimensional effects on the transition from ignition to flame spread in microgravity, Symp. (Int.) Combust. 27 (1998) 2635–2641.
[28] H.-Y. Shih, J.S. Tien, Modeling concurrent flame spread over a thin solid in a low-speed flow tunnel, Proc. Combust. Inst. 28 (2000) 2777–2784.
[29] X. Zhang, Y. Yu, Experimental studies on the three-dimensional effects of opposed-flow flame spread over thin solid materials, Combust. Flame 158 (2011) 1193–1200.
[30] W.R. Hu, J.F. Zhao, M. Long, X.W. Zhang, Q.S. Liu, M.Y. Hou, Q. Kang, Y.R. Wang, S.H. Xu, W.J. Kong, H. Zhang, S.F. Wang, Y.Q. Sun, H.Y. Hang, Y.P. Huang, W.M. Cai, Y. Zhao, J.W. Dai, H.Q. Zheng, E.K. Duan, J.F. Wang, Space program SJ-10 of microgravity research, Microgravity Sci. Technol. 26 (2014) 159–169.
[31] H.G. Zhao, J.W. Qiu, B.C. Tang, Q. Kang, W.R. Hu, The SJ-10 recoverable microgravity satellite of China, J. Space Explor. 4 (2016) 101/1–9.
[32] K. Prasad, Y. Nakamura, S.L. Olson, O. Fujita, K. Nishizawa, K. Ito, T. Kashiwagi, Effect of wind velocity on flame spread in microgravity, Proc. Combust. Inst. 29 (2002) 2553–2560.
[33] S.L. Olson, P.V. Ferkul, J.W. Marcum, High-speed video analysis of flame oscillations along a PMMA rod after stagnation region blowoff, Proc. Combust. Inst. 37 (2019) 1555–1562.
[34] J.D. Buckmaster, G.S.S. Ludford, Lectures on mathematical combustion, SIAM, Philadelphia, 1983.
[35] F. Richecoeur, D. Kyritsis, Experimental study of flame stabilization in low Reynolds and Dean number flows in curved mesoscale ducts, Proc. Combust. Inst. 30 (2005) 2419–2427.

[36] T. Jackson, J. Buckmaster, Z. Lu, D. Kyritsis, L. Massa, Flames in narrow circular tubes, Proc. Combust. Inst. 31 (2007) 955–962.
[37] S.L. Olson, H.R. Baum, T. Kashiwagi, Finger-like smoldering over thin cellulosic sheets in microgravity, Symp. (Int.) Combust. 27 (1998) 2525–2533.
[38] O. Zik, Z. Olami, E. Moses, Fingering instability in combustion, Phys. Rev. Lett. 81 (1998) 3868–3871.
[39] S.L. Olson, F.J. Miller, I.S. Wichman, Characterizing fingering flamelets using the logistic model, Combust. Theory Model. 10 (2) (2006) 323–347.
[40] S.L. Olson, F.J. Miller, S. Jahangirian, I.S. Wichman, Flame spread over thin fuels in actual and simulated microgravity conditions, Combust. Flame 156 (2009) 1214–1226.
[41] S. Wang, S. Wang, K. Zhu, Y. Xiao, Z. Lu, Near quenching limit instabilities of concurrent flame spread over thin solid fuel, Combust. Sci. Technol. 188 (3) (2016) 451–471.
[42] R. Chen, G.B. Mitchell, P.D. Ronney, Diffusive-thermal instability and flame extinction in nonpremixed combustion, Symp. (Int.) Combust. 24 (1992) 213–221.
[43] Z. Lu, A diffusion-flame analog of forward smolder waves: (II) stability analysis, Combust. Flame 196 (2018) 529–542.
[44] O. Zik, E. Moses, Fingering instability in solid fuel combustion: the characteristic scales of the developed state, Symp. (Int.) Combust. 27 (1998) 2815–2820.
[45] C.H. Chen, J.S. T'ien, Diffusion flame stabilization at the leading edge, Combust. Sci. Technol. 50 (1986) 283–306.
[46] Z. Lu, M. Matalon, Structure and dynamics of edge flames in the near wake of unequal merging shear flows, Combust. Theory Model. 20 (2016) 258–295.
[47] K. Ohtake, K. Okazaki, Optical CT measurement and mathematical prediction of multi-temperature in pulverized coal combustion field, Int. J. Heat Mass Transf. 31 (1988) 397–405.
[48] M. Shimoda, A. Sugano, T. Kimura, Y. Watanabe, K. Ishiyama, Prediction method of unburnt carbon for coal fired utility boiler using image processing technique of combustion flame, IEEE Trans. Energy Convers. 5 (1990) 640–645.
[49] M.M. Zhu, H. Zhang, G.T. Tang, Q. Liu, J.F. Lu, G.X. Yue, S.F. Wang, S.X. Wan, Ignition of single coal particle in a hot furnace under normal- and micro-gravity condition, Proc. Combust. Inst. 32 (2009) 2029–2035.
[50] Y. Huang, Y. Yan, Transient two-dimensional temperature measurement of open flames by dual-spectral image analysis, Trans. Inst. Meas. Control 22 (2000) 371–384.
[51] C. Lou, H.C. Zhou, P.F. Yu, Z.W. Jiang, Measurements of the flame emissivity and radiative properties of particulate medium in pulverized-coal-fired boiler furnaces by image processing of visible radiation, Proc. Combust. Inst. 31 (2007) 2771–2778.
[52] M.M. Hossain, G. Lu, Y. Yan, Measurement of flame temperature distribution using optical tomographic and two-color pyrometric techniques, in: IEEE International Instrumentation and Measurement Technology Conference Proceedings, IEEE, Graz, Austria.
[53] B. Müller, U. Renz, Development of a fast fiber-optic two-color pyrometer for the temperature measurement of surfaces with varying emissivities, Rev. Sci. Instrum. 72 (2001) 3366–3374.
[54] J.B. Armstrong, S.L. Olson, J.S. T'ien, Transient model and experimental validation of low-stretch solid-fuel flame extinction and stabilization in response to a step change in gravity, Combust. Flame 147 (2006) 262–277.